Slow group velocity and nonlinear optical effects in a coherently driven hot rubidium gas

Vassilios Kaxiras* and Austin W. Li†

Department of Physics, Harvard University, Cambridge, Massachusetts 02138, USA

(Dated: April 8, 2025)

Rubidium has proven a workhorse for investigations of atomic physics. Its simple and accessible electronic structure has lead to its use as an atomic clock frequency standard, and as a platform for quantum computing and quantum information. In this paper, we provide a characterization of the eight $L = 0$ to $L = 1$ (D1) hyperfine transitions of ^{87}Rb and ^{85}Rb, the lowest order transitions that strongly couple to near-visible light. We use a new proposed model for the spectrum of multiple nearby transitions excited by two counter-propagating beams to extract the Doppler-broadened and inherent line widths of all eight D1 lines, finding relatively good agreement with the literature. Within the $F = 2$ to $F = 1$ D1 transition of ^{87}Rb, we characterize narrow two-photon transitions associated with electromagnetically induced transparency (EIT), finding full line widths as low as 3 KHz. Lastly, we utilize these narrow transitions to demonstrate group velocities in Rb vapor three orders of magnitude less than vacuum.

I. INTRODUCTION

The transition spectrum of the single valence electron of rubidium has been widely studied [1–5], especially in the context of rubidium as a platform for quantum information [6–8]. Rubidium is the 23rd most abundant element in Earth's crust [9] and appears in two naturally occurring isotopes: the stable ^{85}Rb, and the radioactive ^{87}Rb with a half life of 4.9×10^{10} years [10]. In perhaps the most well-known application of rubidium, the hyperfine structure exhibited by the coupling of a non-zero nuclear spin to the electronic angular momentum within the ^{87}Rb isotope has been used to develop extremely stable atomic clocks [11]. These atomic clocks are used as frequency standards in military, scientific, and civilian applications [12]. Beyond this, much work has been devoted to investigating the optical properties of hot rubidium gas [4, 13], which exhibits several interesting phenomena. Firstly, Doppler broadening of electronic transitions due to the random thermal movement of a hot gas can be easily observed in a rubidium gas near and above room temperature. This effect typically prevents investigation of the zero-temperature behavior of such transitions, but in the presence of multiple optical beams exciting the same transitions, it is possible to observe so-called sub-Doppler effects due to saturation of atomic absorption. These sub-Doppler effects reveal properties of the electronic transitions at zero-temperature, such as their line width. Furthermore, dark states, or states from which no transition is optically excited within a certain configuration, have been extensively studied in rubidium [14, 15]. One such interesting dark state can be prepared when light resonant to a pair of degenerate transitions will suddenly experience no absorption due to a quantum-mechanical two-photon coherence effect called a dark res-

onance [14, 16]. Such electromagnetically-induced transparency (EIT) features exhibit extremely high dispersion near resonance, which has been used to slow the propagation of light pulses down to 90 m/s [4]. In this paper, we aim to provide another characterization of the well-known spectrum of rubidium for the naturally-occurring isotopes ^{85}Rb and ^{87}Rb, specifically within the $L = 0$ to $L = 1$ (D1) transition, where L is the electron orbital angular momentum number. We chose to focus on this transition because it is capable of exhibiting interesting sub-Doppler and dark state effects, and it is easily accessible via an inexpensive near-infrared laser.

Our paper is organized as follows. In section II, we provide some relevant theoretical background. In section III, we describe the aspects of our experimental setup common to each of the three investigations we perform into the sub-Doppler spectrum, dark resonances, and slow light properties of rubidium. These three investigations form the last three sections. In our first investigation, we fit the sub-Doppler spectrum of ^{85}Rb and ^{87}Rb to a model we propose based on the semi-classical treatment of individual transitions, and find impressive agreement between theory and experimental data. In our second investigation, we observe the emergence of dark resonances within the ^{87}Rb D1 line with extremely narrow full line widths near 3 KHz, where F is the total atomic angular momentum number. In our third investigation, we utilize the highly dispersive qualities of these narrow dark resonances to reduce the group velocity of a single polarization component of light to a few hundred thousand meters per second.

II. BACKGROUND

A. Properties of rubidium

A diagram of the rubidium hyperfine structure is shown in Fig. 1. Rubidium has one valence electron at $n = 5$, leading to a relatively simple electronic level

---

structure. The electron has an intrinsic spin angular momentum $\boldsymbol{S}$, and an orbital angular momentum $\boldsymbol{L}$. The $\boldsymbol{L}$ states are labelled by the orbital angular momentum number $L = 0, 1, 2, \ldots$ as the $s, p, d, \ldots$ states. In general, an eigenstate of $\boldsymbol{V}^2 \equiv \boldsymbol{V} \cdot \boldsymbol{V}$, where $\boldsymbol{V}$ is an angular momentum operator, has eigenvalue $\hbar^2 V(V+1)$, where V is the corresponding angular momentum number. In this paper, we will focus on transitions between the ground $L = 0$ state $5^2 s_{1/2}$ and the $L = 1$ anti-aligned $\boldsymbol{L}, \boldsymbol{S}$ state $5^2 p_{1/2}$; the so-called D1 line at 794.7 nm. Rubidium has non-zero nuclear spin $\boldsymbol{I}$, with $I = 5/2$ for ^{85}Rb and $I = 3/2$ nuclear spin for ^{87}Rb. This nuclear spin couples to $\boldsymbol{S}, \boldsymbol{L}$ to produce a hyperfine level structure described by the total angular momentum $\boldsymbol{F} \equiv \boldsymbol{I} + \boldsymbol{J} + \boldsymbol{S}$. For ^{87}Rb, this results in $F = 1, F = 2$ manifolds in both ground $(L = 0)$ and excited $(L = 1)$ states, and for ^{85}Rb this results in $F = 2, F = 3$ manifolds in both states.

B. Two-level systems: Semi-classical model

Throughout this paper, we refer to the semi-classical model of atom-light interaction as a guide in our analysis, so we present an overview of the model here.

Consider a two level atomic system of one electron with a ground state $|g\rangle$ and excited state $|e\rangle$, in the presence of a coherent electric field $\boldsymbol{E} = \boldsymbol{E}_0 e^{i(\omega_l t - k_0 x)}$ with frequency ω_l, wave number k_0, and amplitude $\boldsymbol{E}_0$. Treating the atom quantum-mechanically and the field classically, the interaction between the electric field and the atom's electric dipole will have energy $e\boldsymbol{E} \cdot \boldsymbol{r}$, where $-e$ is the charge of the electron. For dipole allowed transitions, where

$$\boldsymbol{r}_{eg} \equiv \langle e|\boldsymbol{r}|g\rangle \neq 0, \tag{1}$$

this leads to a coupling term $\Omega = \frac{e}{\hbar} E_0 |r_{eg}|$ (the Rabi frequency) in the atom's Hamiltonian, in addition to the already existing energy splitting Δ between the two unperturbed states $|g\rangle, |e\rangle$:

$$H = \begin{bmatrix} \Delta/2 & \Omega \cos(\omega_l t) \\ \Omega \cos(\omega_l t) & -\Delta/2 \end{bmatrix}. \tag{2}$$

Solving Schrodinger's equation in the rotating frame of the light, converting the state picture to a density matrix ρ, and introducing a decay rate γ describing spontaneous emission from $|e\rangle$ to $|g\rangle$ produces the so-called Optical Bloch Equations [17], whose solution in the steady state ($\dot{\rho} = 0$) gives

$$\rho_{ee} = \frac{\frac{1}{4}\Omega^2}{\delta^2 + \gamma^2 + \frac{1}{2}\Omega^2} \quad \rho_{eg} = \frac{\frac{\Omega}{2}}{\delta + i\gamma}(\rho_{gg} - \rho_{ee}) \tag{3}$$

where $\delta \equiv \omega_l - \Delta/\hbar$ is called the detuning, and $\rho_{ge} = \rho_{eg}^*$, $\rho_{gg} = 1 - \rho_{ee}$.

Note that in a cloud of N such atoms, the number of atoms in each state N_e, N_g are determined by the on-diagonal components of ρ, as $N_e = N\rho_{ee}$, $N_g = N\rho_{gg}$.

On the other hand, the off-diagonal elements of ρ lead to non-zero atomic dipole moments according to Eq. 1. The sum of the dipole moments d (assuming all atoms are in the same state) of N such atoms in a cloud form the polarization $P = Nd$ of that medium, from which we can extract the electric susceptibility $\chi = \frac{P}{\epsilon_0 E_0}$. The imaginary component of χ gives rise to an absorption coefficient α:

$$\alpha = k_0 \text{Im}[\chi] = k_0 \frac{\hbar}{\epsilon_0 E_0^2} \frac{\Omega^2 \gamma}{\delta^2 + \gamma^2}(N_g - N_e), \tag{4}$$

while the real part affects its index of refraction:

$$n \approx 1 + \frac{1}{2}\text{Re}[\chi] = 1 + \frac{\hbar}{2\epsilon_0 E_0^2} \frac{\Omega^2 \delta}{\delta^2 + \gamma^2}(N_g - N_e). \tag{5}$$

Combining Eqs. 3, 4, 5 gives the functional dependence of Δn, the differential index of refraction, and α on Ω, δ, γ:

$$\alpha \propto \frac{\gamma}{\delta^2 + \gamma^2 + \frac{1}{2}\Omega^2}, \quad \Delta n \propto \frac{\delta}{\delta^2 + \gamma^2 + \frac{1}{2}\Omega^2}. \tag{6}$$

In particular, we see that the effective (half width at half max) line width of the transition is

$$\Gamma \equiv \sqrt{\gamma^2 + \frac{1}{2}\Omega^2} \tag{7}$$

showing the phenomenon known as *power broadening*, whereby the line width is broadened by greater Ω.

III. EXPERIMENTAL SETUP

1. Laser

The light source used in the experiment is a Vortex 6017 tunable external-cavity diode laser. This laser is a Class IIIb device, and is based on the Littman-Metcalf design [19]. A schematic of the laser design is shown in Fig. 2. This design uses a diode laser, diffraction grating, and mirror that form an external cavity. Small changes

(a) ^{87}Rb hyperfine structure and D1 line. (b) ^{85}Rb hyperfine structure and D1 line.
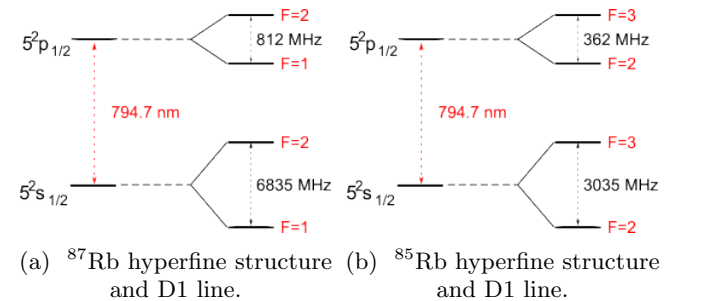
FIG. 1: Hyperfine structure and D1 line of rubidium isotopes.

in the angle of the mirror change the length of the cavity, and thus change the lasing wavelength. Rotation of the end mirror is achieved via a piezoelectric transducer (PZT).

The Vortex controller provides current, voltage, and temperature controls. We keep the laser current at the factory-recommended value of 33.0 mA throughout the experiment in order to prolong the life of the laser and instead vary the voltage setting. The voltage control drives the piezo in the laser head, which controls the lasing wavelength.

2. Rubidium vapor cells

We use two rubidium vapor cells. Each cell is three inches long and one inch in diameter, made from optical quality gas.

One cell contains rubidium vapor of both isotopes, ^{85}Rb and ^{87}Rb. This is the cell mounted at $90°$ to the primary beam axis.

The second cell contains neon buffer gas in addition to rubidium. This buffer gas minimizes collisions of rubidium with the walls. This cell is mounted inside the magnetic shield and solenoid. In particular, this cell contains only ^{87}Rb and 3 Torr of neon gas.

3. Pockels cell

Our setup contains a Pockels cell (Conoptics 350-80LA), which is a voltage-variable wave plate made of a birefringent material. Inside the cell, there is a crystal between two electrodes. We use the Pockels cell to introduce circular polarization and modulate the polarization of light. We then measure the group velocity of light in the modulated circular component. We use a Lasermetrics AF3 DC amplifier to provide a ± 650 V output and modulate the voltage signal using a Gaussian pulse from a Stanford Research Systems DS345 function generator.
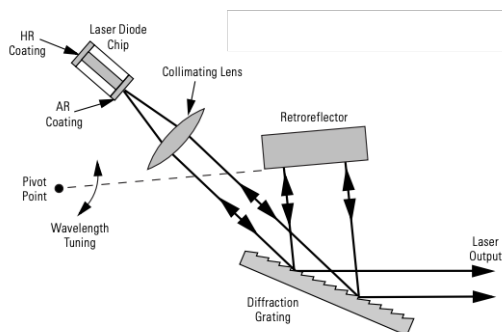

FIG. 2: Littman-Metcalf laser cavity in Vortex 6017 laser [18].

4. Photodetectors

We use both Thorlabs PDA55 and Thorlabs DET110 photodetectors in order to collect our data in the form of beam intensity. The PDA55s require a DC input while the DET110s are battery-powered.

5. Magnetic shield, oven and solenoid

We make use of a three-layer cylindrical mu-metal magnetic shield. A schematic of the shield, oven, and solenoid is given in Fig. 3. This shield screens the rubidium cell containing only ^{87}Rb from the Earth's magnetic field in addition to fields generated in the laboratory. The cylindrical portions of the shield are held together and insulated by sheets of foam.

A heater is wound around the inner cylinder of the shield and heats the cell. A Harrison 6200A regulated DC power supply provides power to the heater. In order to observe dark resonances and detect slow-light signals, we keep the cell at around $60°$ C in order to produce Rb atomic densities in the range of 10^{11} cm^{-3} to 10^{12} cm^{-3}.

Finally, a solenoid is wound on an aluminum frame, consisting of two layers high temperature magnet wire. We vary the strength of the field by driving it via one of the function generators.

IV. SUB-DOPPLER ^{85}Rb AND ^{87}Rb SPECTROSCOPY

A. Theory

The spectral lines of a gas of atoms at finite temperature exhibit so-called Doppler broadening [20]. Atoms with velocity v along the direction of beam propagation will experience the beam frequency Doppler shifted by $\Delta \omega = -vk$, where k is the wave number of the beam.
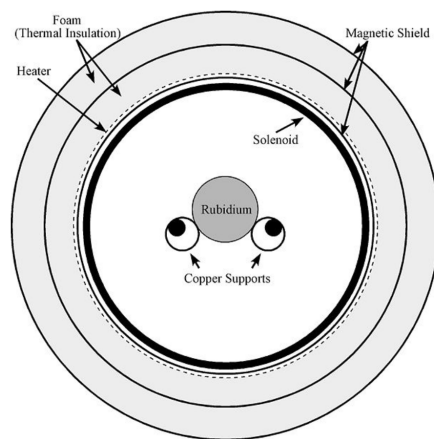

FIG. 3: Magnetic shield, oven, and solenoid schematic.

The distribution of velocities for atomic mass m at temperature T follows the Maxwell-Boltzmann distribution:

$$P(v) = \sqrt{\frac{m}{2\pi k_B T}} e^{-\frac{mv^2}{k_B T}}. \tag{8}$$

The interactions of different velocity classes of atoms with the beam at a given transition results in a broad line width, as a beam with detuning δ will be on-resonant for atoms moving at velocity $-\delta/k$.

Introducing a second, counter-propagating beam produces interesting effects. At the same detuning δ as the pump beam, the probe interacts with atoms in the δ/k velocity class. Thus for $\delta = 0$, these beams interact with the same atoms: those moving in the plane normal to the beams' propagation ($v = 0$). This interaction tends to produce dips in the absorption around $\delta = 0$, as the same atoms absorbing the probe beam are also more likely to be in the excited state (and therefore unable to absorb) due to the pump beam.

Here, we introduce a model for this behavior based on the semi-classical treatment of atom-light interaction. In this model, for a spectrum with n transitions, the population difference between all ground states and all excited states in $N(v)$ atoms of velocity $\boldsymbol{v}$ directly follows from Eq. 3:

$$\Delta N(v) = N(v) \left[1 - \frac{1}{2} \sum_{i=1}^{n} \frac{\Omega_i^2}{(\delta_i - vk)^2 + \gamma_i^2 + \frac{1}{2}\Omega_i^2} \right]. \tag{9}$$

Each transition has its own detuning δ_i, half line width γ_i, and Rabi frequency Ω_i.

From Eq. 4, the probe beam will then experience an absorption coefficient (integrating over all velocity classes) proportional to

$$\int_{-\infty}^{\infty} dv \left[\sum_{j=1}^{n} e^{-\frac{m(v - v_0^{(j)})^2}{k_B T}} \frac{\Omega_j^2 \gamma_j}{(\delta_j + vk)^2 + \gamma_j^2} \right] \Delta N(v) \tag{10}$$

where we have introduced a mean velocity $v_0^{(j)}$ of the jth transition to account for shifts in the sub-Doppler line due to thermal variations in the gas. There are several implicit assumptions in our choices for Eqs. 9 and 10: see Appendix B for a more detailed discussion.

Now we consider terms that give rise to sub-Doppler effects. At $\delta_i = 0$, the "diagonal" terms in the product of the sums

$$\left[\frac{\Omega_i^2}{(vk)^2 + \gamma_i^2 + \frac{1}{2}\Omega_i^2} \right] \left[\frac{\Omega_i^2 \gamma_i}{(vk)^2 + \gamma_i^2} \right] \tag{11}$$

give rise to dips in the absorption at resonance because the point of maximum absorption in the second term ($v = 0$) also corresponds to the point of greatest saturation in the first term, where ΔN is minimized as a function of δ_i.

Of particular interest are the "off-diagonal terms" at $\delta_i = -\delta_j$, when the pump frequency is halfway between
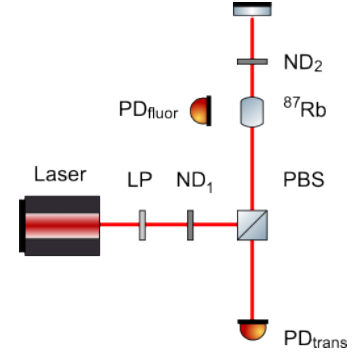

FIG. 4: Laser spectroscopy and Doppler-free saturation spectroscopy schematic.

the resonant frequencies of the i'th and j'th transitions, as this results in

$$\left[\frac{\Omega_i^2}{(\delta_i - vk)^2 + \gamma_i^2 + \frac{1}{2}\Omega_i^2} \right] \left[\frac{\Omega_j^2 \gamma_j}{(-\delta_i + vk)^2 + \gamma_j^2} \right]. \tag{12}$$

Once again, the point of maximum absorption in the second term ($v = \delta_i/k$) also corresponds to the point of greatest saturation in the first term, providing the same dip in absorption. These are known as *crossover resonances*, and predict a phenomenon that we observe in our experimental data. Intuitively, they occur when the pump and probe beam interact with the same group of atoms, but with two different transitions, providing the same absorption saturation effect of on-resonant sub-Doppler peaks, but now at the mean frequency of every pair of transitions.

B. Experimental setup

We investigated the combined spectrum of ^{85}Rb and ^{87}Rb by sweeping the frequency of a linearly polarized beam near the D1 line. This sweep consisted of a triangular waveform on the piezo frequency modulation input of our laser, at a rate of 0.5 Hz. We calibrated the relationship between the frequency modulation and the absolute frequency via comparison of our observed transition peaks to the D1 line detunings between different ground state F manifolds in the literature [2].

A counter propagating probe beam $10^{1.6}$ times weaker in intensity was added to observe sub-Doppler effects. This was achieved by placing an ND 0.8 attenuating filter followed by a mirror after the Rb cell.

Our optical schematic for both laser spectroscopy and Doppler-free saturation spectroscopy is shown in Fig. 4. We used two photodetectors to observe absorption lines in transmission of the probe beam and fluorescence from the pump beam. Additionally, in order to improve the quality of our measurements, we constructed a light shield surrounding the PD$_{\text{fluor}}$ (Fig. 4) and the ^{87}Rb sample.

We tuned the values of the two ND filters in Fig. 4, balancing the noise in the transmission signal (which grew with $ND_1 + 2ND_2$) with the power-broadening of the sub-Doppler features (which grew inversely with the strength of the ND filters), settling on $ND_1 = 0.4$ and $ND_2 = 0.8$.

C. Results

The transmission in PD_{trans} (Fig. 4), denoted T, was manually fitted to the function

$$T(a, b, d, \alpha) = ae^{-d\alpha} + b \tag{13}$$

where α was manually fitted to Eq. 10 for the eight transitions of the zero magnetic field hyperfine ^{85}Rb, ^{87}Rb spectrum. Two additional Doppler-broadened transitions with no sub-Doppler effects were added in the fit at approximately 0 MHz and 2000 MHz detuning, to account for dips in the transmission that were not associated with any transition. These additional dips are present because the true absorption profile of a transition at detuning δ resembles sinc(δ) rather than a Lorentzian [21].

The fit results are shown in Table I and Fig. 5. From the Table, our estimate of the inherent full linewidth 2γ of the D1 transition is approximately 12-60 MHz, depending on the hyperfine manifolds involved. Results in the literature with similar Rb setups find 5 MHz [22]: this discrepancy is due to the power broadening induced by our strong pump beam, which is difficult to separate from the inherent line width.

V. DARK RESONANCES OF ^{87}Rb

A. Theory

Each F manifold in the ^{87}Rb spectrum is spanned by a basis of size $2F + 1$. Absent external interaction terms, these $2F + 1$ states are degenerate in energy. Thus, we can excite them all resonantly, allowing us to investigate a fascinating phenomenon of quantum coherence known as dark resonances.

As a brief overview of the origin of dark resonances, consider the simplest case that can give rise to them: a three-level system, with two degenerate ground states and one excited state, known as a Λ system (Fig. 6). Suppose the two ground states $|1\rangle, |2\rangle$ are coherently driven with strengths Ω_1, Ω_2, and the atom is in general superposition of $|1\rangle, |2\rangle$ with coefficients c_1, c_2. The atom will be driven to the excited state at a total rate of

$$\Omega_1 c_1 + \Omega_2 c_2. \tag{14}$$

In particular, if

$$\frac{c_1}{c_2} = -\frac{\Omega_2}{\Omega_1} \tag{15}$$

there will be no driving to the excited state: this is usually referred to as EIT (electromagnetically induced transparency) [16]. Preparing this state can be done by optically pumping the atom, allowing it to explore all states of the three-level system. Once the atom reaches the dark resonance state, it will be trapped there, as the optical pumping will no longer have any effect. Because the lifetime of this transition depends on the coherence of the ground states rather than the excited state lifetime, this transition can be far narrower than the single-photon resonance at that same frequency. For dark resonances,
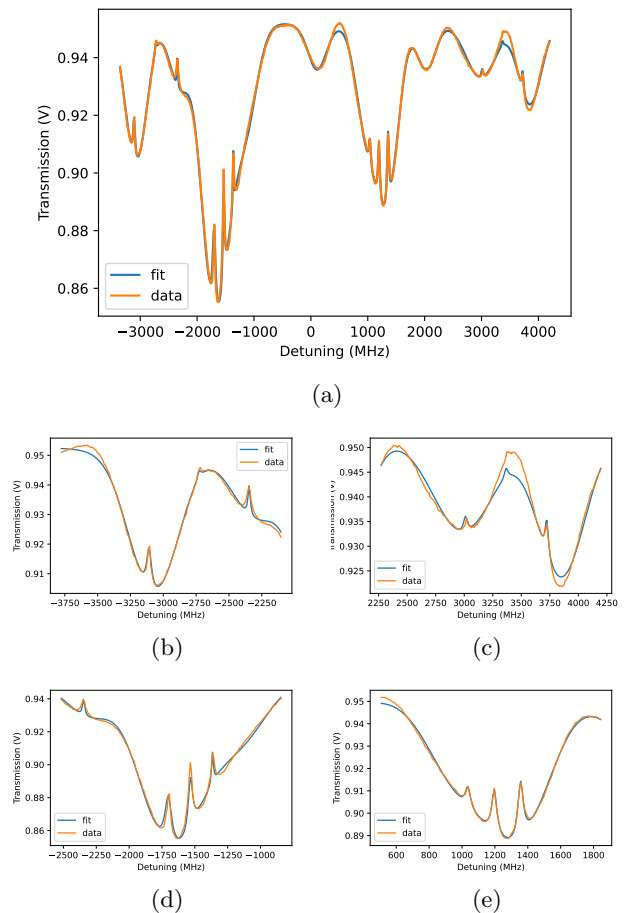
(a)

(b)

(c)

(d)

(e)

FIG. 5: Sub-Doppler rubidium spectroscopy.
(a) The full spectrum of the D1 lines of ^{85}Rb and ^{87}Rb. Spikes in transmission correspond to increased saturation due to both pump and probe beams interacting with the same group of atoms.
In the labels below, g and e refer to the ground ($L = 0$) and excited ($L = 1$) states, respectively.
(b) The ^{87}Rb $F_g = 2$ transitions to $F_e = 1, 2$.
(c) The ^{87}Rb $F_g = 1$ transitions to $F_e = 1, 2$.
(d) The ^{85}Rb $F_g = 3$ transitions to $F_e = 2, 3$, with large crossover resonance located at their midpoint.
(e) The ^{85}Rb $F_g = 2$ transitions to $F_e = 2, 3$, with large crossover resonance located at their midpoint.

TABLE I: Derived properties of the 8 D1 transitions of ^{85}Rb and ^{87}Rb. δ_0 refers to the transition frequency relative to the lowest transition of that isotope, γ is the inherent half linewidth, Ω is the Rabi frequency, v_0 is the mean velocity of the Maxwell-Boltzmann Distribution for that transition, and γ_D is the Doppler-broadened linewidth (half width at half max, as for γ). See Appendix C for error propagation and curve fit.

| | ^{87}Rb | | | |
	$F_g = 2 \to F_e = 1$	$F_g = 2 \to F_e = 1$	$F_g = 1 \to F_e = 1$	$F_g = 1 \to F_e = 2$
δ_0 (MHz)	0 ± 1.0	762.3 ± 1.4	6095.7 ± 3.4	6834.7 ± 1.8
γ (MHz)	18.57 ± 0.98	6.64 ± 1.22	11.68 ± 1.86	7.46 ± 1.05
Ω (MHz)	28.62 ± 0.08	17.32 ± 0.12	16.94 ± 0.09	20.93 ± 0.09
v_0 (m/s)	-27.7 ± 1.0	-32.5 ± 2.4	36.5 ± 3.0	-103.6 ± 1.9
γ_D (MHz)	170.0 ± 1.0	176.0 ± 2.6	241.9 ± 3.0	181.4 ± 1.8
	^{85}Rb			
	$F_g = 3 \to F_e = 2$	$F_g = 3 \to F_e = 3$	$F_g = 2 \to F_e = 2$	$F_g = 2 \to F_e = 3$
δ_0 (MHz)	0 ± 0.6	335.7 ± 0.7	2738.2 ± 1.3	3058.2 ± 0.7
γ (MHz)	33.63 ± 0.77	6.29 ± 0.84	16.27 ± 0.99	14.70 ± 0.70
Ω (MHz)	46.34 ± 0.07	23.31 ± 0.09	24.12 ± 0.11	32.10 ± 0.09
v_0 (m/s)	-22.8 ± 0.6	-145.9 ± 1.8	32.3 ± 1.6	16.8 ± 0.9
γ_D (MHz)	198.2 ± 0.5	208.1 ± 1.8	174.2 ± 1.6	176.5 ± 0.9
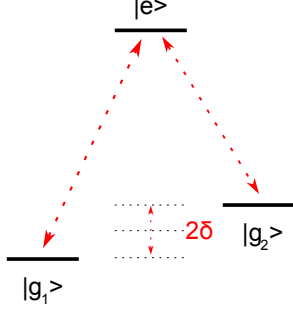
FIG. 6: Three-level Λ system. Assuming a mechanism such as the Zeeman effect that breaks the degeneracy of the ground states, a drive tuned to the mean of the two transitions will be δ red-detuned for $|g_1\rangle$ and $-\delta$ detuned for $|g_2\rangle$.

we expect the dominant decoherence method to be atoms moving beyond the region of the beam, called the "time of flight" (TOF) [23].

One example of such a Λ system corresponds to the two $m_F = \pm 1$ angular momentum z-projection states of some manifold with total angular momentum $F \geq 1$ in the ground state, and a state with $m_F = 0$ in the excited state. Since photons carry total angular momentum 1, resonant circularly polarized light of a particular handedness will excite only one of these states : σ^+ (right handed) light will excite the $\Delta m_F = 1$ transition, and σ^- (left handed) light will excite the $\Delta m_F = -1$ transition [24].

In this Λ system, introducing a non-zero magnetic field B would break the degeneracy of the ground state due to the Zeeman effect, producing a detuning δ for each m_F state:

$$\delta = -g_F \mu_B B_z m_F \qquad (16)$$

where μ_B is the Bohr magneton, B_z is the applied magnetic field, and g_F is the Landé g-factor.

We study the dark resonance around zero magnetic field between $F = 2$ in the ground state to $F = 1$ in the excited state of ^{87}Rb. This state provides three Λ triplets, one for each of $m_F \in \{-1, 0, 1\}$ in the excited state. We chose this state because it provided the highest signal-to-noise ratio in our apparatus.

To characterize the line widths of the dark resonances, we chose to observe their variable dispersion rather than absorption. Looking at Eqs. 4, 5, when $\delta \gg \gamma$ we see that $\alpha(\delta) \propto \delta^{-2}$ and $\Delta n(\delta) \propto \delta^{-1}$ (where $\Delta n \equiv n - 1$); thus it is easier to observe the dark resonance via Δn rather than α because its features will be less sharp. We expect a dependence of the refractive index on the detuning as given in Eq. 6, for a dark resonance width Γ. Denote the refractive index for σ^+ light as n^+, and the refractive index for σ^- light as n^-. To characterize Γ, we probe a dark resonance transition with both circularly polarized components at equal amplitude, i.e. uniformly linearly polarized light. If $n^+ \neq n^-$, the atoms will impart a different phase on the two components: we expect the difference of these two phases to be

$$\Delta\varphi = \frac{c}{\omega}(n_+ - n_-) \propto \frac{\delta}{\delta^2 + \Gamma^2} - \frac{-\delta}{\delta^2 + \Gamma^2} = \frac{2\delta}{\delta^2 + \Gamma^2} \quad (17)$$

where the detuning δ has the opposite sign between the two components as demonstrated in Fig. 6, and ω is the beam frequency.

Assuming such a phase shift $\Delta\varphi$ between the σ^+ and σ^- components of the linearly polarized beam and negligible absorption, we can extract $\Delta\varphi$ by applying a polarizer rotated 45 degrees relative to the axis of the linear polarization. Consider the decomposition of the linear polarized light into circularly polarized components in

the Jones calculus (see Appendix A for an overview)

$$\begin{bmatrix} 1 \\ 0 \end{bmatrix} = \frac{1}{2} \begin{bmatrix} 1 \\ i \end{bmatrix} + \frac{1}{2} \begin{bmatrix} 1 \\ -i \end{bmatrix}. \tag{18}$$

Applying a phase shift $\Delta\varphi$ between the circularly polarized components and multiplying by the transformation matrix of a linear polarizer rotated 45 degrees relative to the original linear polarization gives

$$\frac{1}{2} \begin{bmatrix} 1 & 1 \\ 1 & 1 \end{bmatrix} \left(e^{i\Delta\varphi} \frac{1}{2} \begin{bmatrix} 1 \\ i \end{bmatrix} + \frac{1}{2} \begin{bmatrix} 1 \\ -i \end{bmatrix} \right)$$

$$= \frac{1}{4}(e^{i\Delta\varphi}(1+i) + 1 - i) \begin{bmatrix} 1 \\ 1 \end{bmatrix} \tag{19}$$

$$\approx \frac{1}{4}(2 - (1-i)\Delta\varphi) \begin{bmatrix} 1 \\ 1 \end{bmatrix}$$

for $\Delta\varphi \ll 1$, which we can reasonably expect for low rubidium vapor densities. Thus measuring either polarization will give a signal with intensity linearly dependent on $\Delta\varphi$

$$\approx \frac{1}{4}(1 - \Delta\varphi) + O(\Delta\varphi^2) \tag{20}$$

from which we can extract $\Delta\varphi$.

B. Experimental setup

Our optical schematic for dark resonance observation and analysis is shown in Fig. 4. We note that by placing a sequence of half wave plates and polarizing beam splitter, we are able to select for linear polarization of one orientation. Specifically, the half wave plate before the Rb chamber is used to rotate the horizontally oriented light from the PBS by 45 degrees, making the second PBS perform its projection in this rotated basis as required by Eq. 19. A photodiode placed inline after this beam splitter measures the dispersion signal.

The ^{87}Rb cell used in this setup is kept at 60° C in order to maintain a Rb density of 2.3×10^{11} cm^{-3}, as determined by a model for the vapor pressure in the literature [2].

Moreover, we investigate the effect of laser power on the line width of dark resonances by placing an ND attenuating filter before the Rb cell.
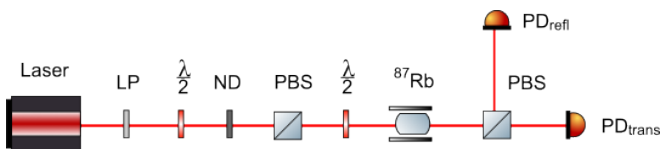

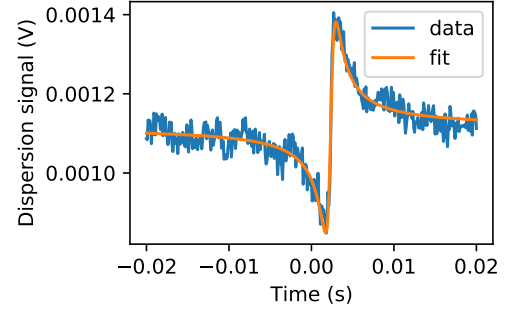FIG. 7: Dark resonance observation schematic.

FIG. 8: Example dark resonance dispersion signal fitted to asymmetric Lorentzian dispersion. We sweep the magnetic field linearly with time.
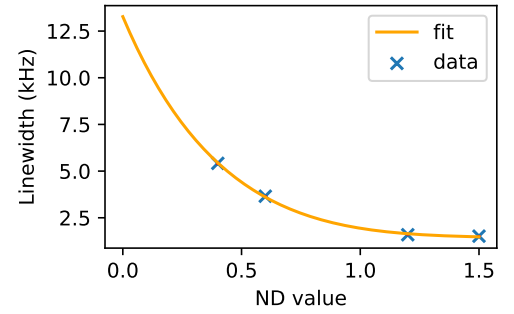

FIG. 9: Dark resonance half line width γ as a function of intensity attenuation. Error bars are shown in red, but are too small to be visible on the plot (see Appendix C for error propagation and curve fit).

C. Results

For each value of the laser power, we extract Γ, the power-broadened width of the dark resonance, via a fit of the dispersion signal to Eq. 17. An example of this is shown in Fig. 8.

We fit Γ as a function of laser power to

$$\Gamma = \sqrt{\gamma^2 + \Omega_0^2 10^{-\beta}} \tag{21}$$

where β is the power attenuation, Γ is the power-broadened half line width, γ is the inherent half line width, and Ω_0 is the Rabi frequency with zero attenuation.

We find that the inherent half line width is given by

$$\boxed{\gamma = 1.419 \pm 0.048 \text{ kHz.}} \tag{22}$$

The plot and fit of the data is shown in Fig. 9. This value agrees very well with the literature: observations of EIT features in a similar setup have been reported with a minimum (half width) linewidth of $\gamma = 1.5$ kHz [22].

VI. SLOW LIGHT IN ^{87}Rb

A. Theory

The group velocity of light in a medium with frequency-dependent index of refraction $n(\omega)$ is

$$v_g = \frac{d\omega}{dk} = \frac{1}{\frac{d}{d\omega}\left(\frac{n\omega}{c}\right)} = \frac{c}{n + \omega\frac{dn}{d\omega}}. \quad (23)$$

Consider the refraction around a dark resonance, for one particular circularly polarized component of light. Assuming the $\Delta n \ll 1$ and $\delta \ll \omega$, from Eq. 6 we obtain

$$\omega\frac{dn}{d\omega} = \omega\frac{Ne^2|r_{eg}|^2}{2\hbar\epsilon_0}\frac{\Gamma^2 - \delta^2}{(\Gamma^2 + \delta^2)^2} \quad (24)$$

because of the narrow line width of the dark resonance and the corresponding steep dispersion, this may be much greater than 1, which makes v_g far less than c. Note that this implies v_g is minimized at $\delta = 0$: in our case, this corresponds to exactly on-resonant light and zero Zeeman splitting.

B. Experimental setup

Our optical schematic for slow light propagation measurement is shown in Fig. 10.

The setup is very similar to the dark resonance line width measurement setup. One key difference is the addition of the Pockels cell, a voltage-dependent polarizer. The beam incident on this polarizer is linearly polarized, and we arrange this polarizer such that modulations to its input rotate the linear polarization, introducing a small amount of the polarization component perpendicular to the primary component. The linear polarization is then converted to elliptical polarization via a quarter wave plate. We modulate the Pockel cell's input voltage signal using a Gaussian pulse from a Stanford Research Systems DS345 function generator. This pulse travels at the group velocity through the Rb vapor, demonstrating the phenomonon of "slow light".

The main polarization component of the beam is rotated to the circular σ^+ polarization by the quarter wave plate. The modulated component perpendicular to the main component is rotated to σ^-, and in conjunction with the σ^+ light pumps the Rb into a dark resonance state. At zero magnetic field, the σ^- then experiences the slow group velocity associated with the steep index of refraction of the narrow dark resonance.
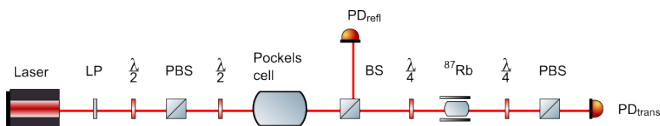

FIG. 10: Slow light observation schematic.

Before entering the rubidium vapor cell, we split the beam with a non-polarizing beam splitter. The reflection is detected by one photodiode, and serves as a reference. The transmission passes through the cell, where it experiences the steep dispersion of the Rb cloud, and is detected by the transmission photodiode.

In our setup we estimated, using the ideal gas law:

$$N = \frac{PV}{k_BT} \approx 1.4 \times 10^{10} \quad (25)$$

where $T = 333$ K is the temperature of the ^{87}Rb cell, P is the rubidium vapor pressure determined from a model in [2], and V is the volume within which there is interaction between the beam and the Rb atoms; V is estimated from the beam width of our laser (0.5 mm) and the length of our Rb chamber (3 inches). The transition dipole element $|r_{eg}| \approx 1.58 \times 10^{-10}$ m for the D1 line is also given by [2], resulting in the following estimate of the group index of refraction:

$$n_g \equiv n + \omega\frac{dn}{d\omega} \approx 3 \times 10^5. \quad (26)$$

Thus for a single circularly polarized component of our beam, we expect group velocities on the order of 10^3 m/s. Finally, we chose the $F = 2$ to $F = 1$ transition of the ^{87}Rb D1 line as our target, as it has the narrowest dark resonances.

C. Results

We first seek to find the group velocity as a function of Zeeman splitting in the $F = 2$ manifold of the ground state. To find the group velocity, we first fit each of our transmitted and reflected pulses to Gaussians of the form

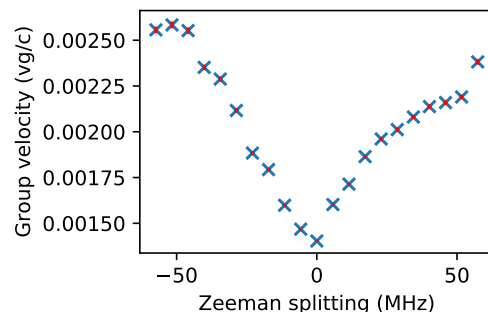$$f(x) = A\exp\left[-\frac{(x - x_0)^2}{2\sigma^2}\right] + f(0) \quad (27)$$

FIG. 11: Group velocity (relative to c) as a function of Zeeman splitting in the $F = 2$ manifold of the $5^2s_{1/2}$ state of ^{87}Rb. Error bars shown in red, but are too small to be visible on the plot (see Appendix C for error propagation and curve fit).

where we seek to extract x_0, the time of the pulse. From the difference of these two values, we can reconstruct the group velocity v_g and corresponding error.

We find that the minimum group velocity $v_{g\min}$ occurs at a Zeeman splitting of 0 as expected, given by

$$v_{g\min} = 4.207 \times 10^5 \pm 1.7 \times 10^3 \text{ m/s,} \qquad (28)$$

which is roughly three orders of magnitude slower than the speed of light in vacuum. Alternatively, we can find the above as a fraction of the speed of light:

$$\frac{v_{g\min}}{c} = 1.4035 \times 10^{-3} \pm 5.6 \times 10^{-6}. \qquad (29)$$

A plot of our data is shown in Fig. 11. Similar setups with hot rubidium gas have observed group velocities as low as 90 m/s, by further optimizing the beam setup and rubidium vapor density [4].

We are also interested in the relationship between group velocity and beam power. We employ the same method above with the Zeeman splitting set to near 0, placing an intensity attenuation filter at the head of our laser, and find that the minimum group velocity $v_{g\min}$ occurs at an intensity attenuation of ND=0.8. The associated group velocity is

$$v_{g\min} = 5.172 \times 10^5 \pm 1.8 \times 10^3 \text{ m/s.} \qquad (30)$$

The corresponding relative velocity is given by

$$\frac{v_{g\min}}{c} = 1.7253 \times 10^{-3} \pm 6.1 \times 10^{-6}. \qquad (31)$$

A plot of our data is shown in Fig. 12. We see that lower beam power (increased ND of the filter) results in higher group velocities, and that above a certain power there is little change in the group velocity.
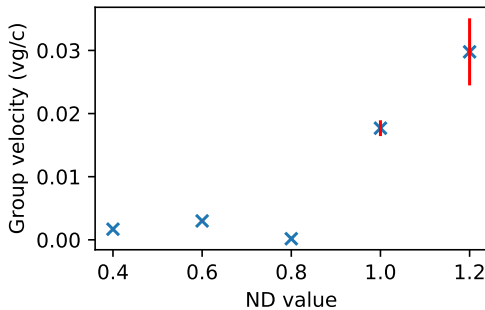
VII.   ACKNOWLEDGEMENTS

FIG. 12: Group velocity (relative to c) as a function of intensity attenuation in the $F = 2$ manifold of the $5^2s_{1/2}$ state of ^{87}Rb. Error bars shown in red (see Appendix C for error propagation and curve fit).

Appendix A: Wave plates and polarizers: Jones calculus

Light polarization is important in this experiment because polarization of light determines selection rules for atomic transitions. Wave plates are used to preferentially retard light along a certain axis, which is achieved by using a material where the index of refraction differs along different axes.

We can represent the transformations of polarizers and wave plates on light using Jones calculus, where polarized light is described by a Jones vector and linear optical elements are represented by Jones matrices. We can define a Jones vector as follows:

$$\begin{bmatrix} E_{0x}e^{i\phi_x} \\ E_{0y}e^{i\phi_y} \end{bmatrix}, \qquad \phi \equiv \boldsymbol{k} \cdot \hat{\boldsymbol{z}} - \omega t \qquad (A1)$$

where $\boldsymbol{k}$ is the wave vector and ω is the angular frequency. It is convention that the wave travels along the $\hat{\boldsymbol{z}}$ axis. Linear polarized light in the $\hat{\boldsymbol{x}}$ and $\hat{\boldsymbol{y}}$ directions are given by

$$|0\rangle \equiv \frac{1}{\sqrt{2}} \begin{bmatrix} 1 \\ 0 \end{bmatrix}, \qquad |1\rangle \equiv \frac{1}{\sqrt{2}} \begin{bmatrix} 0 \\ 1 \end{bmatrix} \qquad (A2)$$

respectively. Circularly polarized light σ^+ (right handed) and σ^- (left handed) are given by

$$|\sigma^+\rangle \equiv \frac{1}{\sqrt{2}} \begin{bmatrix} 1 \\ i \end{bmatrix}, \qquad |\sigma^-\rangle \equiv \frac{1}{\sqrt{2}} \begin{bmatrix} 1 \\ -i \end{bmatrix} \qquad (A3)$$

Any polarized light can be expressed in this basis.

We can define Jones matrices, operators that act on Jones vectors. These matrices are implemented by optical elements like lenses, (polarizing) beam splitters, mirrors, and polarizers.

Polarizers are not unitary; they are projection operators. For a general linear polarizer with axes at an angle θ from the horizontal, the Jones matrix is given by

$$\begin{bmatrix} \cos^2\theta & \cos\theta\sin\theta \\ \cos\theta\sin\theta & \sin^2\theta \end{bmatrix}. \qquad (A4)$$

When θ is 45 degrees, this becomes

$$\frac{1}{2} \begin{bmatrix} 1 & 1 \\ 1 & 1 \end{bmatrix} \qquad (A5)$$

Right and left circular polarizers with their axes along $\hat{x}, \hat{y}$ are given respectively by

$$\frac{1}{2}\begin{bmatrix} 1 & i \\ -i & 1 \end{bmatrix}, \qquad \frac{1}{2}\begin{bmatrix} 1 & -i \\ i & 1 \end{bmatrix}. \tag{A6}$$

Wave plates and phase retarders are rotations and thus unitary operators on Jones vectors. Any linear phase retarder with its axes defined as the $\hat{x}, \hat{y}$ axes has zero off-diagonal terms and can be expressed as

$$\begin{bmatrix} e^{i\phi_x} & 0 \\ 0 & e^{i\phi_y} \end{bmatrix}. \tag{A7}$$

The most general Jones matrix for any arbitrary birefringent material is given by

$$e^{\frac{i\eta}{2}}\begin{bmatrix} \cos^2\theta + e^{i\eta}\sin^2\theta & (1 - e^{i\eta})e^{-i\theta}\cos\theta\sin\theta \\ (1 - e^{i\eta})e^{i\phi}\cos\theta\sin\theta & \sin^2\theta + e^{i\eta}\cos^2\theta \end{bmatrix}. \tag{A8}$$

In this experiment, we use quarter and half-wave plates, with their Jones matrices given by

$$e^{\pm\frac{i\pi}{4}}\begin{bmatrix} 1 & 0 \\ 0 & \pm i \end{bmatrix}, \quad e^{-\frac{i\pi}{2}}\begin{bmatrix} \cos^2\theta - \sin^2\theta & 2\cos\theta\sin\theta \\ 2\cos\theta\sin\theta & \sin^2\theta - \cos^2\theta \end{bmatrix} \tag{A9}$$

respectively.

Appendix B: Sub-Doppler fit assumptions

Our model for the sub-Doppler spectrum of ^{87}Rb (Eq. 10) contains several key assumptions. Here we enumerate them, providing some justifications:

1. The pump beam alone defines the population counts of each excited state. This is approximately correct because the probe beam has $10^{-1.6} \approx 2.5\%$ the intensity of the pump beam.

2. The steady-state excited population count $N_e^{(i)}$ of each transition i can be solved for independently and the total excited state count is the sum of these independent counts. This is justified by considering the fact that no two transitions are significantly overlapping in their sub-Doppler width, so we cannot near-maximally saturate multiple transitions at once.

3. The probe beam experiences the refractive and absorptive qualities of the atoms without altering their states. Again, this is justified by the large intensity difference between the pump and probe beams.

4. The absorption of each transition depends on the total population difference between all excited and all ground states, for any given isotope. This captures the effects associated with both pump and probe beams being on resonant.

Appendix C: Error analysis

We use `scipy.optimize.curve_fit` to calculate error. This curve-fitting technique returns a covariance matrix where the diagonal entries provide the variance of the parameter estimate. Taking the square root of these diagonal entries gives us one standard deviation error, which are the errors we report. Generally, the errors of parameters that are dependent on multiple other parameters are calculated under the assumption of independent, additive variances.

[1] S. Kraft, A. Deninger, C. Trück, J. Fortágh, F. Lison, and C. Zimmermann, Rubidium spectroscopy at 778–780 nm with a distributed feedback laser diode, Laser Physics Letters **2**, 71 (2004).

[2] D. A. Steck, Rubidium 87 d line data, (2001).

[3] D. A. Steck, Rubidium 85 d line data, (2008).

[4] M. M. Kash, V. A. Sautenkov, A. S. Zibrov, L. Hollberg, G. R. Welch, M. D. Lukin, Y. Rostovtsev, E. S. Fry, and M. O. Scully, Ultraslow group velocity and enhanced nonlinear optical effects in a coherently driven hot atomic gas, Physical Review Letters **82**, 5229 (1999).

[5] A. Sargsyan, R. Mirzoyan, and D. Sarkisyan, A study of dark resonance splitting for the d 1 line of 87rb in strong magnetic fields, Optics and Spectroscopy **113**, 456 (2012).

[6] I. I. Ryabtsev, I. I. Beterov, D. B. Tretyakov, V. M. Entin, and E. A. Yakshina, Spectroscopy of cold rubidium rydberg atoms for applications in quantum information, Physics-Uspekhi **59**, 196 (2016).

[7] H. Crepaz, *Trapping and cooling rubidium atoms for quantum information* (2006).

[8] S. Demircan, G. Cui, B. Jordaan, C. Ianzano, and E. Figueroa, Towards cavity-assisted fast rubidium-tuned quantum light sources, in *Quantum 2.0* (Optical Society of America, 2020) pp. QW6A–8.

[9] W. C. Butterman and R. Reese Jr, *Mineral Commodity Profiles–Rubidium*, Tech. Rep. (2003).

[10] G. Audi, O. Bersillon, J. Blachot, and A. H. Wapstra, The nubase evaluation of nuclear and decay properties, Nuclear physics A **729**, 3 (2003).

[11] J. C. Camparo, *The rubidium atomic clock and basic research*, Tech. Rep. (AEROSPACE CORP EL SEGUNDO CA PHYSICAL SCIENCES LABS, 2007).

[12] W. Riley, A history of the rubidium frequency standard, IEEE UFFC-S History , 2 (2019).

[13] L. Weller, R. J. Bettles, P. Siddons, C. S. Adams, and I. G. Hughes, Absolute absorption on the rubidium d1 line including resonant dipole–dipole interactions, Journal of Physics B: Atomic, Molecular and Optical Physics **44**, 195006 (2011).

[14] S. Brattke, U. Kallmann, and W.-D. Hartmann, Coherent dark states of rubidium 87 in a buffer gas using pulsed laser light, The European Physical Journal D-Atomic, Molecular, Optical and Plasma Physics **3**, 159 (1998).

[15] G. Alzetta, L. Botti, S. Cartaleva, A. Rossi, and J. Xu, Hyperfine frequency measurement and interference between different dark states in rubidium 85, Proceedings of SPIE - The International Society for Optical Engineering **4397** (2001).

[16] E. Arimondo, Dark resonances in quantum optics, ACTA PHYSICA POLONICA SERIES A **112**, 723 (2007).

[17] C. Cohen-Tannoudji, eng*Atom-photon interactions : basic processes and applications* (J. Wiley, New York, 1992).

[18] N. Focus, *6000 Vortex Series: User's Guide* (2002).

[19] K. Harvey and C. Myatt, External-cavity diode laser using a grazing-incidence diffraction grating, Optics letters **16**, 910 (1991).

[20] A. E. Siegman, *Lasers* (University science books, 1986).

[21] D. J. Griffiths and D. F. Schroeter, *Introduction to quantum mechanics* (Cambridge university press, 2018).

[22] M. Lukin, M. Fleischhauer, A. Zibrov, H. Robinson, V. Velichansky, L. Hollberg, and M. Scully, Spectroscopy in dense coherent media: line narrowing and interference effects, Physical review letters **79**, 2959 (1997).

[23] R. Wynands and A. Nagel, Precision spectroscopy with coherent dark states., Applied Physics B: Lasers & Optics **68** (1999).

[24] D. Kiang and K. Young, The angular momentum of photons in a circularly polarized beam, American Journal of Physics **76**, 1012 (2008).

[25] G. Heinze, C. Hubrich, and T. Halfmann, Stopped light and image storage by electromagnetically induced transparency up to the regime of one minute, Physical review letters **111**, 033601 (2013).